

An optical study on spray and combustion characteristics of oxymethylene dimethyl ether (OMEx)/n-dodecane blends using an ECN Spray D injector

Downloaded from: https://research.chalmers.se, 2026-11-28 14:25 UTC

Citation for the original published paper (version of record):

Sun, Z., Donkers, G., Dam, N. et al (2026). An optical study on spray and combustion characteristics of oxymethylene dimethyl ether
(OMEx)/n-dodecane blends using an ECN Spray D injector. Proceedings of the Combustion Institute, 42. http://dx.doi.org/10.1016/j.proci.2026.106640

N.B. When citing this work, cite the original published paper.

research.chalmers.se offers the possibility of retrieving research publications produced at Chalmers University of Technology. It covers all kind of research output: articles, dissertations, conference papers, reports etc. since 2004. research.chalmers.se is administrated and maintained by Chalmers Library

(article starts on next page)

Proceedings of the Combustion Institute 42 (2026) 106640

Contents lists available at ScienceDirect

Proceedings of the Combustion Institute

journal homepage: www.elsevier.com/locate/proci

An optical study on spray and combustion characteristics of oxymethylene dimethyl ether (OME_x)/n-dodecane blends using an ECN Spray D injector

Zhongcheng Sun [a,b,*], Gijs Donkers [a], Nico Dam [a], Bart Somers [a], Noud Maes [a]

[a] Department of Mechanical Engineering, Eindhoven University of Technology, Eindhoven, 5600MB, Netherlands
[b] Department of Mechanical Engineering, Chalmers University of Technology, Gothenburg, 412 96, Sweden

ARTICLE INFO

Keywords:
Oxymethylene dimethyl ether
Spray D injector
Constant-volume combustion chamber
Spray combustion
Soot

ABSTRACT

An optical investigation of combustion and soot-reduction characteristics for oxymethylene dimethyl ether (OME_x)/n-dodecane blends is conducted on a high-pressure combustion chamber, using a Spray D injector under ECN boundary conditions. The results illustrate how OME_x blends exhibit a shorter ignition delay relative to n-dodecane, which is attributed to its high fuel-bound oxygen content facilitating lower stoichiometric equivalence ratios. Also, the onset of high-temperature reactions enable occur at higher equivalence ratios because of high reactivity of OME_x. Spray flames of OME_x blends perform a notably extended flame lift-off length compared to n-dodecane flames at low ambient temperature (around 850 K), while the differences are negligible at temperatures above 900 K. This is ascribed to a shift in the flammable limit of OME_x toward lower air–fuel ratio regions compared to n-dodecane, controlled by the ignition kinetics of OME_x, while it might be erroneously as attributed to the lower flame temperature of OME_x related to its lower heating value. Conversely, the similar lift-off length of these two fuels at ambient temperatures above 900 K originates from higher air-fuel ratios around the lift-off length. In all cases, OME_x exhibits a distinct bright-blue flame during the premixed combustion, and a blue-violet flame in the quasi-steady phase, confirming the absence of soot formation. The noticeably thinner and straighter flame structures compared to n-dodecane, along with the increased OH* chemiluminescence near the flame centerline, indicate that OME_x combustion characteristics influenced by local air–fuel ratios are fundamentally different.

Novelty and significance statement: This manuscript explores the combustion and soot-reduction characteristics for OME_x/n-dodecane blends conducted on a high-pressure combustion chamber, using an Engine Combustion Network Spray D injector (representative for heavy-duty engines). This work first validates that OME_x exhibits a distinct bright-blue flame during the premixed combustion and a blue-violet flame in the quasi-steady phase, confirming soot-free combustion. The insights obtained will further advance the understanding of the physico-chemical processes underlying the combustion of OME_x in engines, providing a hypothesis for ignition behavior and flame lift-off length, considering chemical reactivity and equivalence ratio distributions. Especially the extended lift-off length observed at lower temperatures is investigated, which might be erroneously attributed to the lower flame temperature of OME_x. This work is expected to generate significant interest within the community, as synthetic renewable (blended) OME_x fuels offer a sustainable pathway for decarbonization and effective emission reduction in transportation with minimal engine modifications.

1. Introduction

Global emissions and de-fossilization targets are forcing the transition of energy systems toward renewable, low-carbon sources [1]. Although exhaust gas emissions by road traffic are improved with the rise of electric vehicles, internal combustion engines remain essential in agriculture, long-distance transport, marine, and developing economies [2].

Along with advancements in state-of-the-art compression ignition engines, sustainable fuels are required. Oxymethylene dimethyl ether (OME_n), a promising fuel solution, which is characterized by the chemical formula $CH_3O(CH_2O)_nCH_3$ lacks C—C bonds and features a high oxygen content. This reduces, or even completely avoids, soot formation during combustion [3]. In this study, OME_x, a mixture of

* Corresponding author at: Department of Mechanical Engineering, Eindhoven University of Technology, Eindhoven, 5600MB, Netherlands.
E-mail address: z.c.sun@tue.nl (Z. Sun).

https://doi.org/10.1016/j.proci.2026.106640
Received 14 March 2026; Accepted 19 June 2026
Available online 10 October 2026
1540-7489/© 2026 The Author(s). Published by Elsevier Inc. on behalf of The Combustion Institute. This is an open access article under the CC BY license (http://creativecommons.org/licenses/by/4.0/).

OME_n compounds (where n = 3–6), is used. OME_x exhibits excellent ignitability with a high cetane number (CN=82), significantly exceeding the EN590 minimum standard [4]. However, potential challenges arise in some practical scenarios, since the lower heating value (LHV) of OME_x is nearly half that of diesel, requiring a larger fuel tank to maintain a certain range, and injectors and/or injection strategy require modifications [5]. Therefore, it could be relevant to use OME_x as a blend component in diesel engine applications, considering its diesel-like properties with strong soot-reduction potential. Recently, a comprehensive evaluation using a wide range of OME_x blend ratios was conducted on a heavy-duty engine, indicating that an OME_x ratio of around 24 vol% can achieve diesel-like engine efficiency while meeting Euro VI PM and Euro V NO_x regulations without aftertreatment [6,7]. Existing studies highlight how the high oxygen content of OME_x leads to a reduction in required air entrainment for complete combustion [8]. Rajasegar et al. substantiated this by their observation of a spatially wider OH* chemiluminescence distribution of OME_x fuel compared to n-dodecane (nC12, a surrogate fuel for diesel) in an optical engine, independent of ambient oxygen concentration [9]. Several studies have investigated OME_x fuels within the framework of the Engine Combustion Network (ECN) [10–17]. These studies found that the vapor penetration of OME_x using a Spray D injector (186-μm nominal diameter, representative for heavy-duty engine applications) show greater variability than Spray A injector with smaller diameter (90-μm nominal diameter), also highlighted in ECN workshop discussions [18]. Moreover, flame lift-off length (LOL) and ignition delay (ID) are important parameters related to the combustion process, and there are also some discrepancies in these parameters for Spray D injectors [19]. This underscores the importance of extended experimental investigations of combustion involving OME_x fuels.

In this work, multiple optical diagnostic techniques are employed simultaneously to enable a detailed analysis of critical combustion parameters under engine-like conditions, including ID and LOL. Additionally, the flame structure and transient combustion and soot characteristics of OME_x and OME_x/nC12 blends are investigated. This work aims to enhance the understanding of low-soot combustion associated with OME_x-based fuels and provide insights for engine development to meet future emission regulations.

2. Experimental methodology

2.1. Experimental methodology

The experiments are conducted under engine-like conditions in a constant-volume combustion chamber employing various optical techniques, see Fig. 1. A brief description is provided here; details can be found in [20]. The vessel used is an optically accessible pre-burn combustion chamber with six window ports of 100 mm diameter each. The desired experimental conditions are achieved by burning a specifically designed gas mixture, ignited by commercial automotive spark plugs. This mixture is composed of acetylene, argon, nitrogen, and oxygen.

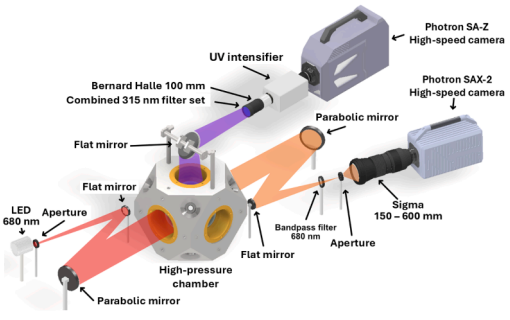

Fig. 1. Experimental setup of the high-pressure chamber with the representative optical arrangement.

Fuel is injected into chamber by a Spray D injector, pressurized using a syringe pump, during the relatively long cool-down period of the pre-combustion, at the instant when the ambient pressure and temperature match the desired condition. Injection duration is set to 5 ms.

Fuel spray penetration under both inert and reacting conditions is captured using Schlieren imaging [21]. A Z-type schlieren optical arrangement is utilized in this work, as illustrated in Fig. 1. A 6-W continuous wave LED (CREE, 680 nm) serves as the point source. The light reflects off a flat mirror and is directed towards a parabolic mirror (6-inch diameter, 1200-mm focal length) to form parallel light passing through the vessel. Following a mirrored arrangement, the transmitted light passes through a narrow bandpass filter centered at 680 nm (10-nm FWHM), and is collected by a high-speed CMOS camera (Photron SA-X2) equipped with a Sigma 150–600 mm f/5.0–6.3 zoom lens. A second high-speed CMOS camera (Photron SA-Z) coupled to a high-speed intensifier (Invisible Vision 1850–05 UVi) was used to collect OH* chemiluminescence (high-speed OH*) through a 100-mm UV objective (Bernhard Halle Nachfl. f/2) equipped with a combination of filters (Semrock FF01–315/15–50 & FF01–300/80–50) to maximize transmission at 310 nm while minimizing soot incandescence. A flat-field correction was applied to mitigate pixel-to-pixel sensitivity variations and vignetting caused by the intensifier [22]. Both OH* chemiluminescence and Schlieren images post-processing primarily follow ECN guidelines [10]. Natural luminosity (NL) imaging is utilized to examine soot distribution. These images are captured using a third high-speed CMOS camera (Photron SA-X2) equipped with a Sigma 105-mm f/2.8 EX lens and a 600-nm long-pass filter (Andover 600FH90–50). The specific camera configurations of optical techniques are summarized in Table 1. Furthermore, true-color flame images were captured using a high-speed color camera (Photron Nova-S6), to compare the sooting behavior of tested fuels. The frame rate is set to 20,000 frames per second, with exposure times set to 50 μs for OME_x and 1.05 μs for nC12.

2.2. Fuel preparation and experimental design

Fuel properties of OME_x and nC12 are provided in previous work [6,20]. To simplify the naming convention, OME_x25 denotes a blend of 25% OME_x and 75% nC12. OME_x8, OME_x25, and OME_x50 are tested in this work, in addition to OME_x and nC12. The ambient temperature (T_a) is set to 850, 900, and 950 K, while the ambient pressure (P_a) is calculated using the ideal gas law, with ambient density fixed at 22.8 kg/m^3. The injection pressure (P_{inj}) is fixed at 100 MPa, and ambient oxygen content (O_2) is set to 0 and 15 vol.%.

3. Results and discussion

3.1. Ignition delay and lift-off length

The ID and LOL of OME_x-nC12 blends are presented in Fig. 2. ID data, obtained from high-speed OH* chemiluminescence recordings, shows a good agreement with other ECN institutions (Sandia and CMT) at the standard condition (900 K) with Spray D injector [18], as shown in insert figure in Fig. 2. It is clear that ID decreases with increasing OME_x content, which is expected based on the cetane number and consistent with engine research findings [6]. In this work, the uncertainties of the

Table 1
Specific camera configurations.

	Schlieren	High-speed OH*	NL
Camera	SAX-2	SA-Z	SAX-2
Frame rate (fps)	40,000	40,000	40,000
Resolution (pixel)	896 × 368	1024 × 512	896 × 368
Pixel/mm	9.67	8.08	9.67
Exposure time (μs)	15.05	23.38	0.29

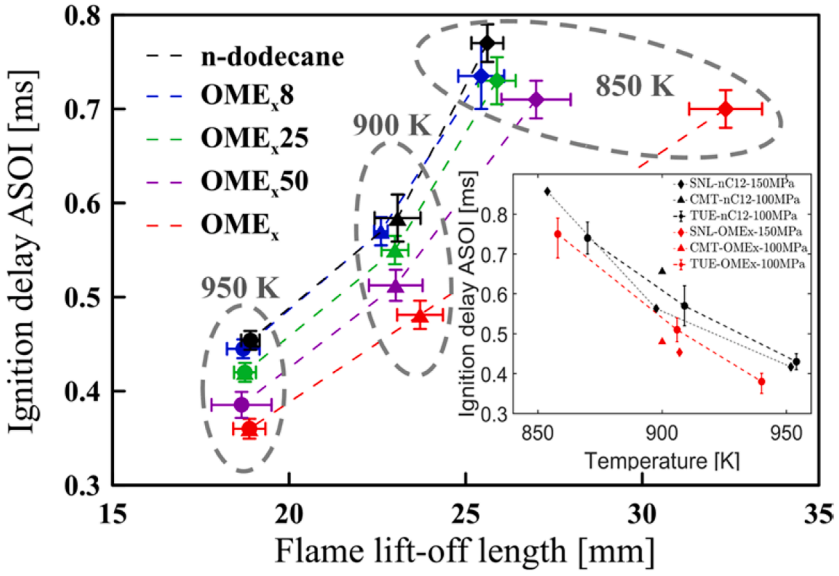

Fig. 2. Relationship between ID and LOL using the Spray D injector at different ambient temperatures.

10-injection ensemble-averaged ID and LOL were 6.5% and 2.3%, respectively, with 95% confidence intervals falling within the corresponding standard deviations.

ID comprises both a physical contribution (e.g., evaporation and mixing) and an Arrhenius-type chemical contribution. The former is strongly influenced by OME_x because of the high oxygen content, which facilitates an ignitable mixture more rapidly—even under low ambient oxygen concentrations—due to the reduced stoichiometric air-fuel ratio (AFR_{st}) than nC12 [23]. Note that evaporation is limited by the rate of air entrainment under diesel engine conditions [24]. The latter, the chemical part of ID, is also shorter for OME_x [25]. OME_x exhibits only a weak negative temperature coefficient (NTC) behavior during low-temperature reactions [25], distinguishing it from compounds like nC12. This weak NTC effect accounts for the limited sensitivity of ID to temperature increasing, especially when the OME_x concentrations exceed 50% [26].

Numerical results for the temperature evolution of high-temperature ignition of OME_x with varying equivalence ratio (φ) are provided in Fig. 3 (left panel), while the high- and low-temperature ID with varying φ are illustrated in the right panel. Both panels are obtained from a homogeneous reactor simulation in Chem1D [27] (T_a = 900 K, P_a = 60 bar). The evaporation enthalpy of OME_x is accounted for when determining the fuel vapor temperature. The initial temperature of the mixture at each equivalence ratio φ was determined based on the mixture composition and enthalpy, using adiabatic linear air–fuel mixing. Results show that the onset of high-temperature ignition of OME_x occurs at an equivalence ratio φ = 1.8 (the blue-boxed region in Fig. 3), which is higher than that of nC12 (φ=1.4) [28]. This indicates that OME_x exhibits elevated high-temperature reactivity when compared to nC12 at higher equivalence ratio regions.

Despite the advanced ignition, OME_x exhibits a longer LOL than nC12 (Fig. 2), especially at low temperature of 850 K. The extended LOL benefits air–fuel mixing and reduces the equivalence ratio upstream of the flame, thereby suppressing soot formation. Although the LOL trend resembles that of ID as ambient temperature varies, the underlying mechanisms differ. Fig. 4 presents normalized I_{xt} plots of the spatio-temporal combustion profiles for OME_x and nC12 at 850 and 900 K, highlighting the differences in LOL between the two fuels. The I_{xt} plot is obtained by integrating the OH* intensity distribution $I(x, y, t)$, along

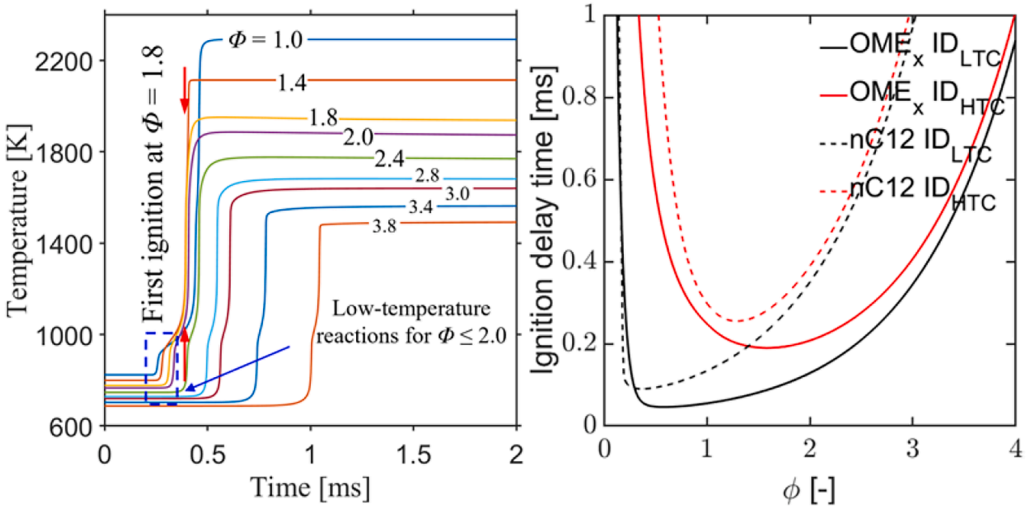

Fig. 3. Left: temperature evolution of pure OME_x for various equivalence ratios φ; Right: high-temperature ID and low-temperature ID profiles with varying φ for nC12 and OME_x. Both panels are obtained from homogeneous reactor simulations (T_a = 900 K, P_a = 60 bar).

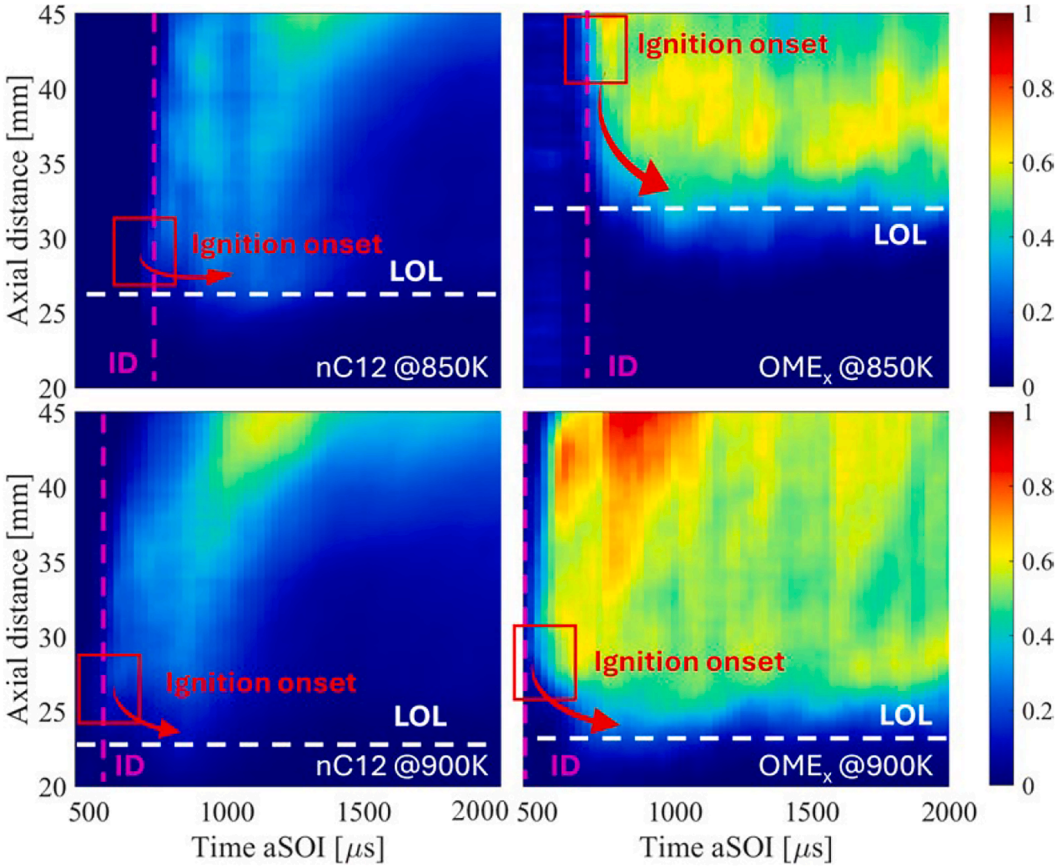

Fig. 4. Normalized radially integrated OH* intensity (I_{xt}) of nC12 and OME$_x$, as a function of axial distance and time, at 850 K and 900 K. ID, ignition onset location, and LOL are identified in the individual panels.

radial flame direction (y) according to: $I_{xt} = \int_{y_{min}}^{y_{max}} I(x,y,t)dy$, providing insight into flame evolution along the axial direction (x) over time (t) after the start of injection (ASOI) [29]. ID, ignition onset location, and LOL are also indicated in Fig. 4.

At low temperature (~850 K), OME$_x$ exhibits a shorter ignition delay than nC12 ($ID_{OMEx} < ID_{nC12}$), as mentioned above. However, the ignition location determined from the onset of OH* chemiluminescence is significantly farther downstream for OME$_x$ (~40 mm) compared to nC12 (~27 mm). This apparent discrepancy is attributed to the combined influence of evaporation and reactive mixture distribution. The downstream shift is hypothesized to result from the increased enthalpy entrainment from the surrounding hot air, which is required for fuel evaporation and reactive mixture formation at lower temperatures, due to the relatively high latent heat of OME$_x$. In addition, the lower AFR_{st} leads to lower equivalence ratios within the spray, considering the similar entrainment rates for OME$_x$ and nC12. After ignition, the onset of OH* signal rapidly moves upstream, likely due to the formation of a more reactive mixture in regions with a higher local equivalence ratio than that of nC12, as supported by chemical kinetic simulations. Subsequently, in the quasi-steady combustion phase, OME$_x$ sustains a longer LOL compared to nC12, which is primarily attributed to its elevated local mixture fraction and a relatively slower mixing rate, as diesel-like combustion is governed by mixing-controlled processes and the spatial development of reactive mixtures. Evidence from Rayleigh-scattering-based mixture fraction measurements [11] indicates that compared to nC12, a higher mixture fraction is observed in OME$_x$ jets initially before 30 mm, while exhibiting a similar mixture distribution further downstream. Additionally, the mixing time for a stabilized air-fuel mixture, estimated by a counter-flow reactor, is longer for OME$_x$ [30]. A similarly extended LOL for OME$_x$ under low-temperature conditions, independent of injector configuration, has also been reported in the literature [16, 30]. However, this behavior has sometimes been erroneously attributed to the lower flame temperature of OME$_x$ related to its lower LHV [31]. In fact, the thermal energy in a diesel-like mixing-limited flame originates from the entrained air and transport of reaction product via turbulence, rather than thermal energy released from the flame itself, which is unlikely to travel upstream. For nC12, the LOL remains closer to its ignition onset, indicating minimal spatial separation between ignition and flame stabilization, aligning with literature [32,33].

When the ambient temperature reaches up to 900 K, ID of OME$_x$ decreases more sharply than that of nC12. This results in approximately a 7% reduction in ID relative to nC12, thereby narrowing the difference in ignition onset location between OME$_x$ and nC12. This is because OME$_x$ tends to ignite at higher equivalence ratios and exhibits a weaker NTC effect than nC12, as discussed above. Although LOL for OME$_x$ still retracts a bit relative to the ignition onset, the reduced distance between them is likely associated with the combined effects of enhanced fuel reactivity and altered local mixing conditions (higher fuel–air ratios), compared to the 850 K case. Consequently, OME$_x$ and nC12 exhibit similar LOL under these high temperature conditions.

3.2. *Effect of OME$_x$ on flame morphology*

The normalized spatiotemporal combustion profiles for nC12, OME$_x$25, and OME$_x$ are shown in Fig. 5. OMEx25 was selected based on previous engine studies, due to its lower emissions [7]. OME$_x$ exhibits the shortest ID, as illustrated by the purple dashed line. The ignition timing closely aligns with the point at which the gradient of vapor penetration (V_p, yellow dashed line) begins to change, due to the

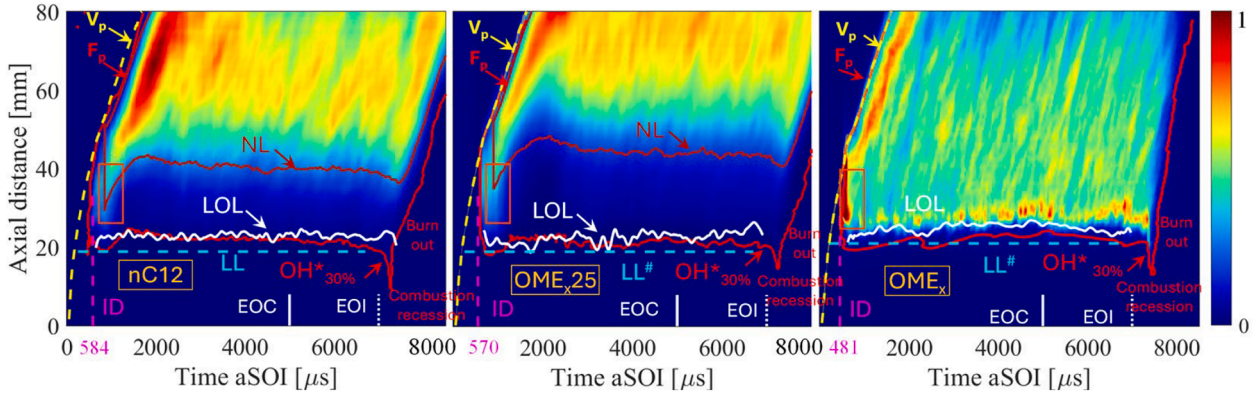

Fig. 5. Normalized radially integrated OH* intensity (I_{xt}) of nC12, OME$_x$25, and OME$_x$, as a function of axial distance and time (T_a= 900 K, O_2 = 15 vol%). Various features illustrated in the figures support the analysis provided in the text.

thermal flame expansion [34]. The schlieren-derived vapor penetration of all tested fuels is similar, while the steady-phase spray angle slightly decreases with OME$_x$ addition, consistent with [12]. The liquid length (LL, cyan line) is determined from Mie-scattering induced by natural luminosity. The liquid phase remains detectable up to an OME$_x$ ratio of 25%, beyond which the luminosity is insufficient for detection. Therefore, LL of OME$_x$ (LL$^{\#}$) is estimated from previous Mie-scattering data using its proportionality to injector diameter [35]. The slightly longer liquid length of OME$_x$ may be due to its higher density [36].

After ignition, a short spike (highlighted by red boxes) is observed, corresponding to the premixed combustion phase, which is particularly pronounced for OME$_x$ compared to the other fuels. Its short duration is attributed to the shorter ID of OME$_x$, which limits the amount of fuel available for premixed combustion. The stronger OH* signal primarily results from the lower local equivalence ratio in the fuel jet relative to nC12, due to the high intrinsic oxygen content of OME$_x$, thereby promoting premixed combustion. This is presumably related to a higher fuel consumption rate during the premixed phase, as corroborated by the premixed combustion peak observed in the apparent heat release rate profiles from engine experiments [6]. In addition, OH* intensity is highly sensitive to OME$_x$ decomposition pathways [37], as contributed by reaction H + O_2 ↔ O + OH and the chain-branching reaction CH_3 + HO_2 ↔ CH_3O + OH [8]. The elevated OH* intensity is further supported by the numerical results presented in the following sections. Subsequently, the LOL (white line) gradually stabilizes. Flame penetration, defined by the 30% threshold of the initial peak OH* intensity, is observed in the upper-left region of I_{xt} plot. Despite combustion-induced expansion, flame penetration (F_p) closely aligns with vapor penetration (V_p). Furthermore, the downstream OH* apparently higher for nC12 and OME$_x$25 than for OME$_x$, due to interference from soot incandescence [29]. To substantiate this claim, soot-dominant regions for these two fuels are identified using a 15% threshold of the peak NL intensity, where dark red contours indicate regions with reliably detectable soot incandescence. It is observed that the most upstream soot location of nC12 during the quasi-steady combustion phases is closer to the injector than that of OME$_x$25, illustrating the soot-reduction effect of OME$_x$ addition. Although the LP filter strongly attenuates wavelengths below 600 nm, weak transmission combined with sufficiently high light intensity can still enable partial detection of chemiluminescence. Thus, the NL limit of OME$_x$ is more close to the LOL than nC12, primarily caused by this NL signal arising from chemiluminescence contributions [38,39]. Furthermore, long-wavelength H_2O vapor emission above 600 nm may represent an additional contributing factor [40].

After the end of injection (EOI), OME$_x$ exhibits a weaker combustion recession than nC12, which could be due to its low AFR_{st}, resulting in overly lean mixtures for sustaining combustion or signal strength below the detection limit. Finally, OME$_x$ exhibits a faster burn-out compared to nC12, again presumably because of its low AFR_{st}, given that this phase is governed by the local equivalence ratio [41].

Fig. 6 presents spatial–temporal composite images (without spatio-temporal correspondence) of nC12, OME$_x$25, and OME$_x$, to compare their transient flame structures. The gray contours represent vapor-phase fuel identified from Schlieren, while simultaneously measured OH* and NL signals are superimposed in red and green, respectively. These signals are reconstructed as 2D projections from line-of-sight integrated measurements above and below the spray axis using inverse Radon transformation, assuming an axisymmetric flame around the spray centerline [29]. The individual two-dimensional slice $f(r)$ of OH* and NL signal is obtained by: $f(r) = -\frac{1}{\pi}\int_r^R \frac{F'(y)}{\sqrt{(y^2-r^2)}}dy$, where r is the distance to the spray centerline, y is the projection of r on the slice, R is the radius of the slice, and $F'(y)$ is derivative of the line-of-sight integrated signal against y. The intensity of OH* and NL signals are normalized by their respective maximum values at each instant. As illustrated in the first row of Fig. 6, OME$_x$ exhibits higher OH* intensity values near the centerline compared to nC12 and OME$_x$25. Additionally, the onset of high-temperature reactions occurs at higher equivalence ratios, as discussed. Owing to combustion-induced thermal expansion, OME$_x$ exhibits strong OH* emissions across the entire jet at 675 μs, with OME$_x$25 showing a comparable spatial distribution.

As combustion progresses into the diffusion phase at approximately 875 μs, a conical frustum-shaped OH* structure envelops the spray core. Simultaneously, NL signals—associated with soot radiation and visualized in green—emerge for both nC12 and OME$_x$25. Regions where OH* and NL emissions overlap turn yellow in these composite visualizations. Notably, OME$_x$ exhibits peak intensity OH* emission near the LOL, and elevated OH* levels sustained at the spray center fuel-rich regions. Given the soot-free characteristics of OME$_x$ [6,26], isolated luminous spots inside the spray potentially originate from chemiluminescence contributions formed in high-temperature reaction regions. In contrast, NL of nC12 is detected further upstream than OME$_x$25, consistent with the dark red contours in Fig. 5, indicating a larger soot formation region. The reduced NL in OME$_x$25 underscores a reduction in soot formation primarily due to OME$_x$ addition rather than significant alterations in nC12 reaction pathway [26].

During the quasi-steady combustion phase at approximately 1550 μs, the OH*-based flame morphology with OME$_x$ addition becomes noticeably more contracted compared to that of nC12, adopting a columnar rather than conical shape. This geometric transformation is again attributed to the reduction in the local air–fuel ratio at the spray core—promoting the formation of a more flammable mixture which is unattainable for nC12 at those locations. The higher reactivity of OME$_x$ potentially results in thinner and straighter flames than nC12, likely through interactions between ignition kinetics, local mixing. Furthermore, the non-sooting nature of OME$_x$ minimizes radiative heat losses,

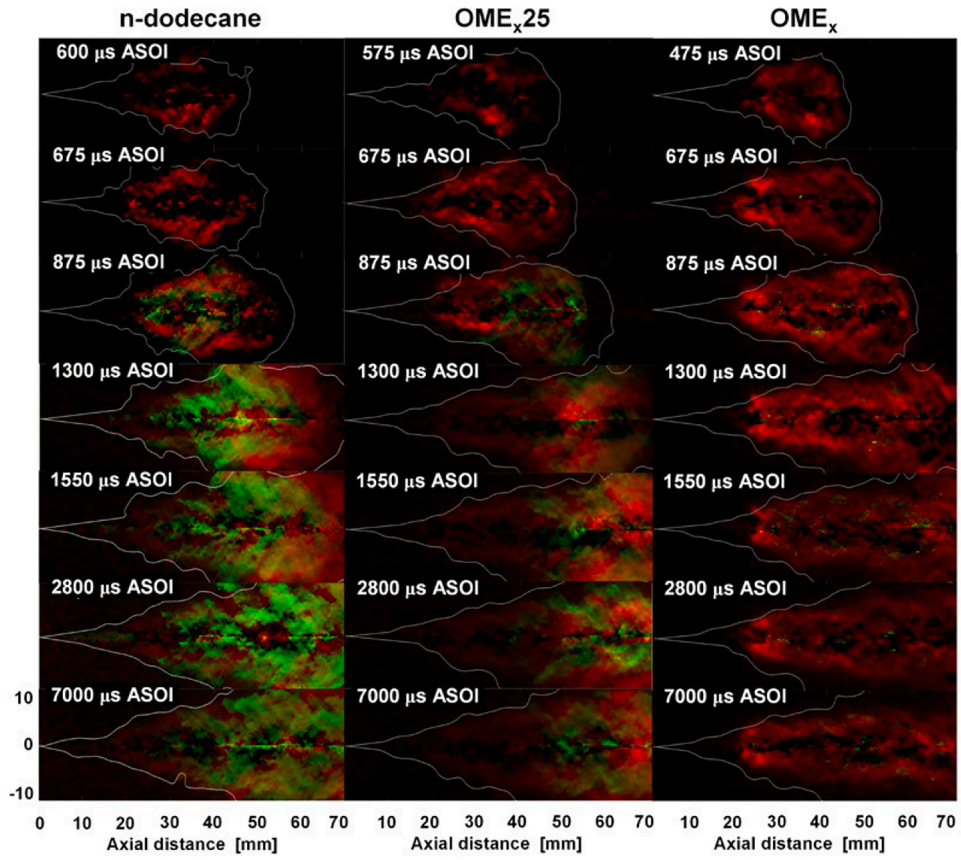

Fig. 6. 2D projections of transient flame structure of OH* (red) and NL (green), overlaid by Schlieren contours (gray) for nC12, OME_x25, and OME_x with a Spray D injector at $T_a = 900$ K, $O_2 = 15$ vol%.

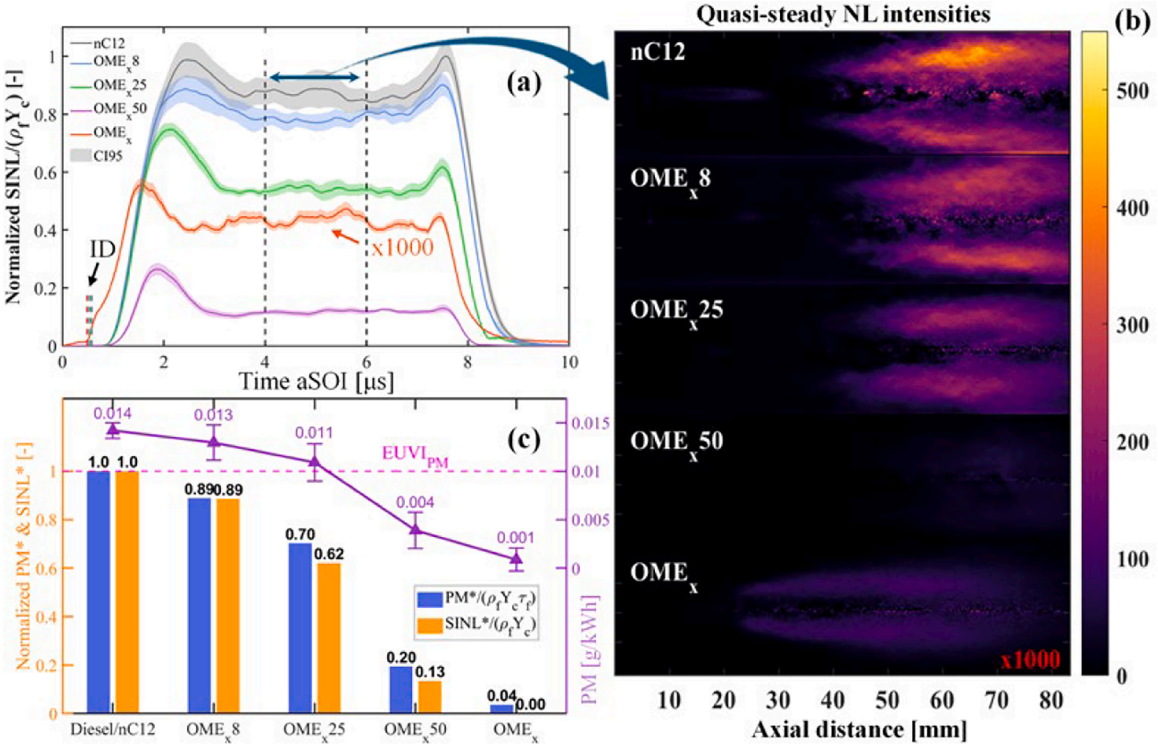

Fig. 7. (a): Normalized SINL time-evolution for fuels at $T_a = 900$ K; (b): Ensemble-average quasi-steady NL intensities of test fuels; (c) Comparison of normalized soot-related metrics (PM*, SINL*) from engine and combustion chamber at quasi-steady phase, with raw engine-out PM values at the top (purple triangles) [6].

reinforcing these distinctive flame characteristics. All these effects contribute to an accelerated combustion rate and a narrower jet envelope.

3.3. Soot propensity of OME_x blends

The time-resolved spatially integrated natural luminosity (SINL) is presented in Fig. 7(a), which is normalized by fuel density (ρ_f) and inherent carbon mass fraction (Y_c), to decouple the influence of fuel-bound carbon content, which is directly correlated with soot mass reduction. Obviously, the normalized SINL, SINL*, for OME_x is approximately three orders of magnitude lower than that of other fuels. The quasi-steady NL intensities—represented as ensemble-averaged images reconstructed via an inverse Radon transformation over the 4–6 ms ASOI time frame—are depicted in Fig. 7(b), suggesting that soot concentration becomes nearly undetectable when the OME_x ratio reaches 50%. Moreover, the NL signal of OME_x appears near the ignition timing, supporting it is presumed to originate from chemiluminescence.

A comparison between the SINL* at the quasi-steady phase and the engine-out particulate matter (PM*) from a prior study is presented in Fig. 7(c), following a similar approach to that described in [26]. Overall, the trend in soot reduction with increasing OME_x content observed in SINL* mirrors that of PM*, exhibiting an exponential decline. Notably, the SINL* and PM* values for OME_x25 are both over 30% lower than those for nC12 and diesel, exceeding the 15% reduction that would be expected based solely on the lower inherent carbon content of OME_x. This consistent trend across other OME_x blends suggests that the soot-reducing effect is not merely a consequence of fuel composition but also indicative of fundamental changes in combustion behavior induced by OME_x.

In Fig. 8, the true-color flame images are accompanied by equivalence ratio distributions computed using a 1D mixing model at the corresponding time instances [41], calibrated using vapor penetration results. The red triangle indicates the injector location. The spray cone angles used in the 1D model were adjusted within 2° of the experimental schlieren measurements to match the vapor penetration of inert sprays [30]. The first row of flame images in Fig. 8 corresponds to 150 μs after the ID for each fuel. To enhance visibility, a gamma correction of 0.4 was applied to the nC12 image. Notably, OME_x exhibits a distinct bright-blue flame during the premixed combustion phase. This blue hue is hypothesized to preliminary originate from a broad CO continuum emission, likely originating from the reaction $CO + O \rightarrow CO_2 + h\nu$ [38], and a part superimposed CH* chemiluminescence contribution in the high-temperature zones near stoichiometric conditions [39], or water vapor [40]. Note that this imaging setup is insensitive to UV light. The equivalence ratio for the OME_x is provided by simulation results, which indicate values well below two in the reaction zone. Although these simulations are for non-reactive spray conditions, the predictions remain qualitatively relevant to the early stages following ignition [41]. In contrast, the nC12 flame—visible in the upper portion—exhibits a near-orange hue, expectedly due to soot incandescence. This is consistent with equivalence ratio estimates, which suggest a richer air–fuel mixture for nC12.

At approximately 1550 μs, when combustion transitions into the quasi-steady phase, the blue hue of the OME_x flame is observed predominantly near the LOL. This emission gradually transitions to a more bluish-violet hue moving downstream. The flame structure of OME_x stays contracted. The calculated equivalence ratio panels in Fig. 8 provide further insights into soot formation, where φ_{LOL} represents the cross-sectionally averaged equivalence ratio at LOL [29]. LOL is indicated by a dashed white line in Fig. 7. It is necessary to highlight that the presented 1D model cannot capture the evolution of the equivalence ratio under reacting conditions, as it does not include chemical kinetics. The equivalence ratio is resolved based on mass and momentum conservation, through the radial profiles validated by the vapor penetration and fuel volume-fraction profiles [42]. Considering the minor difference

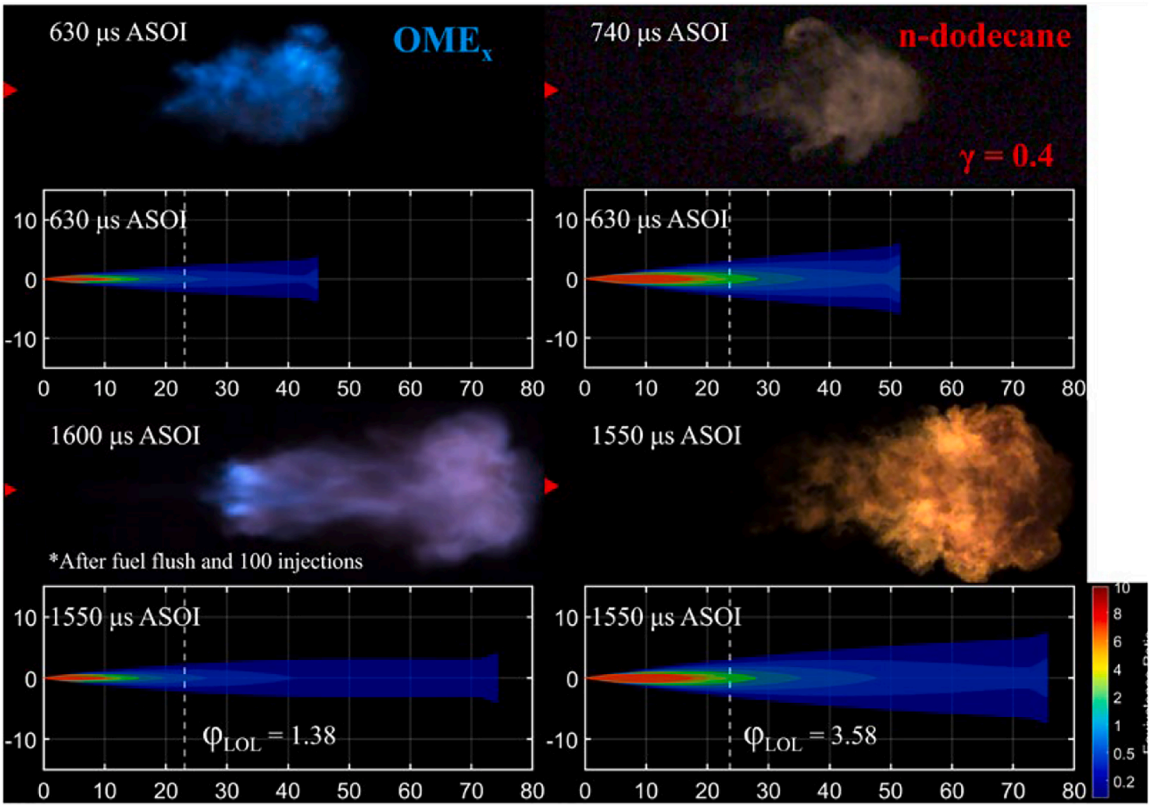

Fig. 8. True-color flame photographs and corresponding equivalence ratio distributions from the 1D spray model. The first row of images shows the flames at 150 μs after the ignition delay for both fuels. The second row shows the quasi-steady phase at 1550 μs.

for spray profiles and vapor penetration between reacting and inert conditions, it is believed that the calculated equivalence ratio distribution results can still be used as a reference for qualitative comparison in reacting conditions, at least up until the lift-off length. For OME_x fuel, the low equivalence ratio near LOL suppresses soot formation and shapes the distinct flame structure previously discussed. In striking contrast, nC12 regions near the spray center exhibit much higher equivalence ratios, leading to more intense soot incandescence.

Equivalence ratio versus temperature maps (φ–T maps) for nC12 and OME_x are given in Fig. 9. The evolution of auto-igniting counterflow diffusion flames (purple dotted lines) is simulated using the Chem1D code [27], with kinetic mechanisms of nC12 and OME_x adopted from [25,43]. High-temperature ignition is initiated in the region of maximum reactivity, corresponding to the trajectory of peak flame temperatures, indicated by the red dashed lines. Although both fuels exhibit similar overall structures in their φ–T maps, the ignition pathway for OME_x initiates at a higher equivalence ratio corresponding to a lower temperature than nC12. This shift is consistent with prior observations in Fig. 3 and can be attributed to the elevated oxygen content, which results in a lower stoichiometric ratio for OME_x. Consequently, the most reactive mixtures occur in relatively fuel-rich regions compared to nC12. Additionally, the φ–T maps are overlaid with contours of OH radical mass fractions, given OH's critical role in high-temperature reactions and soot oxidation chemistry. OME_x exhibits higher peak OH concentrations and a wider distribution than nC12. On the other hand, soot (represented by pyrene here) and NO_x peninsulas are depicted in Fig. 9, computed using the boundary conditions described earlier with a constant temperature homogeneous reactor. Notably, no pyrene is detected for the OME_x fuel, and only a minimal concentration of acetylene (C_2H_2) appears during ignition evolution when the equivalence ratio exceeds 2. It is recognized that soot formation necessitates the nucleation and growth of polycyclic aromatic hydrocarbons (PAHs), which serve as molecular precursors typically generated via the hydrogen-abstraction–carbon-addition (HACA) mechanism [44]. The absence of pyrene thus reinforces the conclusion that soot formation is effectively suppressed during OME_x combustion. In contrast, a significant level of pyrene is observed in nC12 combustion which is considered to be associated with soot nucleation. Similarly, its C_2H_2 distribution spans a wider range of conditions, compared to OME_x. Finally, the distribution of NO_x emissions appears comparable for both fuels. NO_x formation is mostly due to the thermal pathway and depends primarily on the temperature on the lean side of the flame.

To better evaluate the impact of air–fuel mixing and flame temperature on soot production in OME_x blends, the reciprocal of oxygen ratio (Ω) is used, defined as φ_Ω, $\varphi_\Omega = \frac{\varphi_{LOL}}{1+(\varphi_{LOL}-1)\cdot\Omega_f} = \frac{1}{\Omega}$, where Ω_f represents the intrinsic oxygen mole fraction of the fuel [45]. φ_Ω is more suitable than the equivalence ratio φ for characterizing the mixing process, as it considers the fuel-bound oxygen content. Additionally, previous studies show that for OME_x–nC12 blends at 15 vol% O_2 and 900 K, φ_Ω deviates from φ by more than 6% for OME_x25 and up to 10% for OME_x50, suggesting a notable shift in stoichiometry and oxygen availability [30]. A correlation for soot formation rate proposed by Axelbaum and Law is introduced as $\omega \sim X_{F,O}^{a} \cdot exp(-E_a/R_u T_{ad})$ [46], where $X_{F,O}$ represents the fuel concentration in the co-flow diffusion flame, and T_{ad} is the

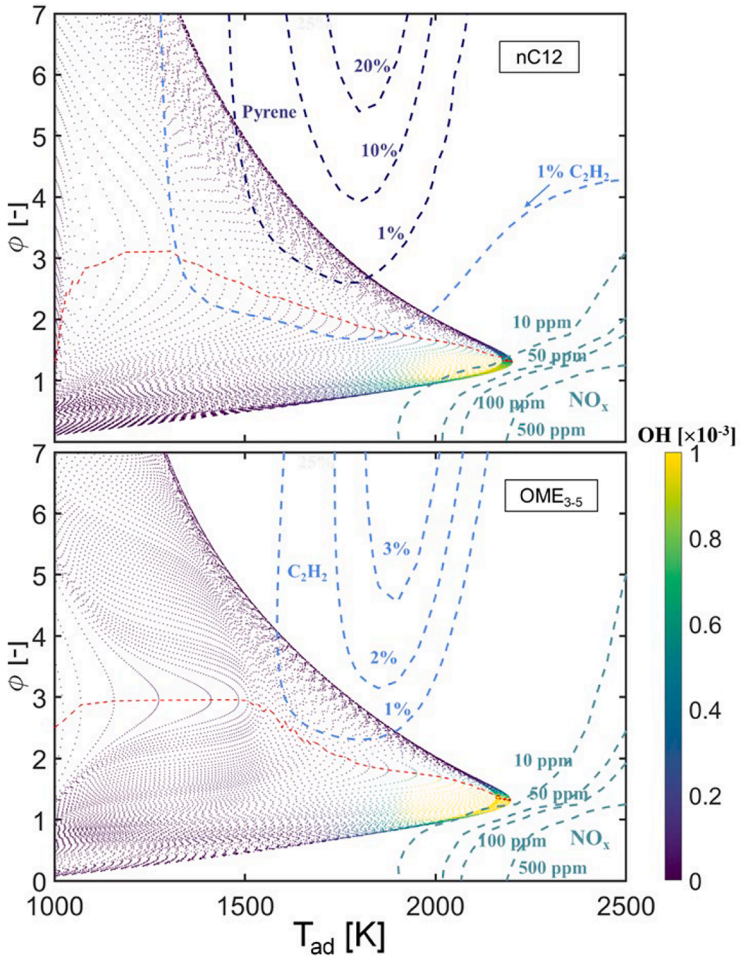

Fig. 9. Temperature evolution of counterflow flames as function of equivalence ratio for nC12 and OME_x, Soot-NO_x peninsulas are obtained from homogeneous reactor simulations (phi-T maps). Both are at T_a = 900 K and P_a = 60 bar.

stoichiometric adiabatic flame temperature. In this work, soot formation rate ω is assumed to remain constant during the quasi-steady combustion phase. Therefore,

$$\omega = \frac{dI_{steady}}{dt} \sim \varphi_{\Omega}^{a} \cdot exp(-E_a / R_u T_{ad}) \quad (1)$$

where the soot formation rate ω is derived from the rising slope of SINL ($\frac{dI_{steady}}{dt}$) during the initial rise stage [26]. The activation energy E_a is taken as 209 kJ/mol, which accounts for the influence of temperature and dilution on the integrated soot volume fraction [46]. The exponent a is assumed to be unity in this work, based on the observation that normalized ω exhibits an approximately linear relationship with φ_{Ω} . Furthermore, SINL is assumed to be directly proportional to the soot concentration [44], considering the T_{ad} of OME_x is comparable to that of nC12, as corroborated by counterflow flame simulations (T_a = 900 K, P_a = 60 bar) [30].

Accordingly, the normalized soot formation rate ωcan be expressed by $\omega = \omega_{\varphi_{\Omega}} \cdot \omega_T$, as presented in Fig. 10. Here, $\omega_{\varphi_{\Omega}}$ is computed by fixing T_{ad} at 2050 K, as obtained from the counterflow flame simulations, whereas ω_T is determined by setting the normalized $\omega_{\varphi_{\Omega}}$to unity. By separately examining the contributions of $\omega_{\varphi_{\Omega}}$ and T_{ad} to soot formation rate, it is observed that soot formation is primarily influenced by φ_{Ω} when its normalized value exceeds 0.27 (i.e., $\varphi_{\Omega} > 1.8$), as the tendency of $\omega_{\varphi_{\Omega}}$is closer to ω. In addition, the authors' earlier combustion chamber studies also confirmed that, at a given oxygen ratio, the SINL* reduction is similar for all OME_x blends within the soot-detectable regions [26]. In contrast, at lower values of φ_{Ω} (below 1.8), T_{ad} has a stronger influence on the soot formation rate, as indicated by the deviation between $\omega_{\varphi_{\Omega}}$and ω. However, under these low φ_{Ω} conditions, no soot formation is detected from experimental results. Note, the soot formation rate correlation employed here does not incorporate detailed chemical kinetics. Consequently, the regression analysis may not fully represent the complexity of the actual soot formation process. Nevertheless, good agreement with experimental data supports that the soot formation rate is more sensitive to φ_{Ω} than to T_{ad} under the conditions examined in this study.

4. Conclusion

This study primarily reports on an optical investigation of combustion and soot-reduction characteristics of OME_x/nC12 blends using a Spray D injector under ECN conditions. Compared with nC12, the shorter ID of OME_x is primarily attributed to its high fuel-bound oxygen content. With similar entrainment rates, its lower stoichiometric air–fuel ratio leads to lower equivalence ratios within the spray. The high reactivity of OME_x enables the onset of high-temperature reactions at higher equivalence ratios than for nC12. The reduced sensitivity of ignition delay to ambient temperature in OME_x is linked to a diminished NTC behavior. Moreover, OME_x exhibits a notably extended LOL compared to nC12 at 850 K. This behavior is primarily governed by the mixing process, which produces a more reactive mixture in regions with higher local equivalence ratios than nC12. Furthermore, the flammability limit of OME_x shifts toward richer conditions relative to nC12, driven by its ignition kinetics. Conversely, the similar LOL of these two fuels originates from higher air-fuel ratios around the LOL when temperatures reach above 900 K. Furthermore, OME_x exhibits narrower, straighter flame structures with respect to the spray axis, with enhanced OH* chemiluminescence intensity near the flame centerline compared to nC12. For OME_x25, a significant shift towards the OME_x flame structure is readily observed. Importantly, OME_x shows a distinct bright-blue flame during the premixed combustion phase and a blue-violet flame during the quasi-steady phase. Its non-sooting behavior, also confirmed by the φ–T maps, suggests that the soot-reducing effect is not merely a consequence of reduced molecular carbon content, but also fundamental changes in combustion characteristics. Lastly, the rate of soot formation is found to be more sensitive with the reciprocal of the oxygen ratio than local flame temperature.

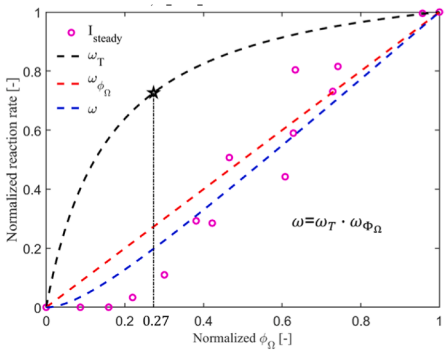

Fig. 10. The relative influence of the φ_{Ω} and T_{ad} on the soot formation rate.

CRediT authorship contribution statement

Zhongcheng Sun: Writing – original draft, Formal analysis, Conceptualization. **Gijs Donkers:** Investigation. **Nico Dam:** Writing – review & editing, Supervision. **Bart Somers:** Writing – review & editing, Supervision. **Noud Maes:** Writing – review & editing, Supervision, Conceptualization.

Declaration of competing interest

The authors declare that they have no known competing financial interests or personal relationships that could have appeared to influence the work reported in this paper.

Acknowledgements

The first author acknowledges financial support from the China Scholarship Council (CSC) Scholarship, as well as support from Prof. Mats Andersson, Prof. Andrei Lipatnikov, and the Swedish Energy Agency.

References

[1] S. Zhang, W. Chen, Assessing the energy transition in China towards carbon neutrality with a probabilistic framework, Nat. Commun. 13 (2022) 1–15.
[2] D. Raimi, Y. Zhu, R.G. Newell, A. Bergman, Global energy outlook 2023: sowing the seeds of an energy transition, Resour. Future 1 (2023) 1–44.
[3] J.M. Ngugi, S. Richter, M. Braun-Unkhoff, C. Naumann, U. Riedel, A study on fundamental combustion properties of oxymethylene ether-2, J. Eng. Gas. Turbine Power. 144 (2022) 011014.
[4] EU: Fuels: Automotive Diesel Fuel. https://dieselnet.com/standards/eu/fuel_automotive.php.
[5] D. Pélerin, K. Gaukel, G. Wachtmeister, Potentials to simplify the engine system using the alternative diesel fuels oxymethylene ether OME1 and OME3–6 on a heavy-duty engine, Fuel 259 (2020) 116231.
[6] Z. Sun, H. Beers, M. Cuijpers, B. Somers, N. Maes, Design of experiments optimized OMEx-diesel blends on a heavy-duty engine – part 1: combustion and emissions analysis with EGR and injection timing variation, Fuel 381 (2025) 133392.
[7] Z. Sun, H. Beers, M. Cuijpers, L.M.T. Somers, N. Maes, Design of experiments optimized OMEx-diesel blends on a heavy-duty engine – part 2: engine performance and exhaust particle analysis with EGR variation, Fuel 388 (2025) 134435.
[8] J.V. Pastor, J.M. García-Oliver, C. Micó, F.J. Tejada, Characterization of the oxymethylene ether fuels flame structure for ECN spray A and spray D nozzles, Appl. Energy 332 (2023) 120475.
[9] R. Rajasegar, A. Srna, Understanding the ignition process and flame structure of conventional and oxygenated fuels under engine relevant conditions–an optical study, Proc. Combust. Inst. 40 (2024) 105682.
[10] https://ecn.sandia.gov/ecn-data-search/.
[11] F. Wiesmann, L. Strauß, S. Rieß, J. Manin, K. Wan, T. Lauer, Numerical and experimental investigations on the ignition behavior of OME, Energies. (Basel) 15 (2022) 6855.
[12] L. Strauß, S. Rieß, M. Wensing, Mixture formation of OME3– 5 and 1-octanol in comparison with diesel-like Dodecane under ECN spray A conditions, Front. Mech. Eng. 9 (2023) 1083658.

[13] L. Strauß, L. Weiß, S. Rieß, M. Wensing, Injection, mixing and auto-ignition of E-fuels for compression ignition engines, MTZ Worldwide 85 (2025) (2024) 54–57.
[14] S. Riess, T. Fuchs, L. Strauß, M. Wensing, Comparison of different injector nozzles for the utilization of polyoxymethylene dimethyl ethers, SAE Tech. Pap. (2024) 4297.
[15] J.V. Pastor, J.M. García-Oliver, C. Micó, A.A. García-Carrero, A. Gómez, Experimental study of the effect of hydrotreated vegetable oil and oxymethylene ethers on main spray and combustion characteristics under engine combustion network spray a condition, Appl. Sci. 10 (2020) 5460.
[16] J.V. Pastor, J.M. García-Oliver, C. Micó, A.A. García-Carrero, An experimental study with renewable fuels using ECN Spray A and D nozzles, Int. J. Engine Res. 23 (2022) 1748–1759.
[17] J.V. Pastor, A. García, C. Micó, F. Lewiski, Simultaneous high-speed spectroscopy and 2-color pyrometry analysis in an optical compression ignition engine fueled with OMEX-diesel blends, Combust. Flame 230 (230) (2021) 111437.
[18] https://ecn.sandia.gov/ecn-workshop/search-presentations/?table_filter=8-Sep%20OME%20and%20Methanol.
[19] N. Maes, S.A. Skeen, M. Bardi, L.M. Malbec, G. Bruneaux, L.M. Pickett, K. Yasutomi, G. Martin, Spray penetration, combustion, and soot formation characteristics of the ECN Spray C and Spray D injectors in multiple combustion facilities, Appl. Therm. Eng. 172 (2020) 115136.
[20] N. Maes, The life of a spray, Ph.D. Thesis, Eindhoven University of Technology, Netherlands, 2019.
[21] G.S. Settles, M.J Hargather, A review of recent developments in schlieren and shadowgraph techniques, Meas. Sci. Technol. 28 (2017) 042001.
[22] J.A. Seibert, K.K Lindfors, Flat-field correction technique for digital detectors, Med. Imaging Phys. Med. Imaging 3336 (1998) 348–354.
[23] Z. Sun, R. Coolen, Y. Wang, M. Cuijpers, B. Somers, N. Maes, Combustion characteristics of oxymethylene dimethyl ether-diesel blends: an experimental investigation using a constant-volume combustion chamber, Fuel 360 (2024) (2024) 130587.
[24] D.L. Siebers, Scaling liquid-phase fuel penetration in diesel sprays based on mixing-limited vaporization, SAE Trans. (1999) (1999) 703–728.
[25] B. Niu, M. Jia, Construction of reduced oxidation mechanisms of PODE with consistent structure using decoupling methodology and reaction rate rule, Combust. Flame 232 (2021) 111534.
[26] Z. Sun, S.K. Peram, B. Somers, N. Maes, The impact of oxymethylene dimethyl ether (OMEx)-diesel blends on combustion and soot-reduction characteristics: experimental and kinetic investigations, Proc. Combust. Inst. 41 (2025) 105908.
[27] L.M.T. Somers, The simulation of flat flames with detailed and reduced chemical models, Ph.D. Thesis,, Eindhoven University of Technology,, Netherlands, 1994.
[28] R.N. Dahms, Paczko, L.M. Pickett, Understanding the ignition mechanism of high-pressure spray flames, Proc. Combust. Inst. 36 (2017) 2615–2623.
[29] N. Maes, N. Dam, B. Somers, T. Lucchini, G. Hardy, Heavy-duty diesel engine spray combustion processes: experiments and numerical simulations, SAE Technical Pap. 1 (2018) 1–22.
[30] Z. Sun, A pathway to sustainable fuels, Ph.D. Thesis,, Eindhoven University of Technology, Netherlands, 2025.
[31] Y. Ma, X. Ma, J. Wang, Optical study on spray combustion characteristics of PODE/diesel blends in different ambient conditions, Fuel 272 (2020) 117691.
[32] L.M. Pickett, S. Kook, H. Persson, Ö Andersson, Diesel fuel jet lift-off stabilization in the presence of laser-induced plasma ignition, Proc. Combust. Inst. 32 (2009) 2793–2800.
[33] L.M. Pickett, D.L. Siebers, C.A. Idicheria, Relationship between ignition processes and the lift-off length of diesel fuel jets, SAE Trans. 1 (2005) 1714–1731.
[34] R. Payri, F.J. Salvador Rubio, G.C. Bracho León, A.A. Viera Sotillo, Vapor phase penetration measurements with both single and double-pass schlieren for the same injection event, in: Ilass Europe, 28th European Conference on Liquid Atomization and Spray Systems, 2017, pp. 747–754.
[35] D.L. Siebers, Scaling liquid-phase fuel penetration in diesel sprays based on mixing-limited vaporization, SAE Trans. 1 (1999) 703–728.
[36] S. Kook, L.M. Pickett, Liquid length and vapor penetration of conventional, Fischer–Tropsch, coal-derived, and surrogate fuel sprays at high-temperature and high-pressure ambient conditions, Fuel 93 (2012) 539–548.
[37] L. Cai, S. Jacobs, R. Langer, F. vom Lehn, K.A. Heufer, H. Pitsch, Auto-ignition of oxymethylene ethers (OMEn, n= 2–4) as promising synthetic e-fuels from renewable electricity: shock tube experiments and automatic mechanism generation, Fuel 264 (2020) 116711.
[38] W. Hwang, J. Dec, M. Sjöberg, Spectroscopic and chemical-kinetic analysis of the phases of HCCI autoignition and combustion for single-and two-stage ignition fuels, Combust. Flame 154 (2008) 387–409.
[39] B. Kim, M. Kaneko, Y. Ikeda, T. Nakajima, Detailed spectral analysis of the process of HCCI combustion, Proc. Combust. Inst. 29 (2002) (2002) 671–677.
[40] P.F. Coheur, P.F. Bernath, M. Carleer, R. Colin, O.L. Polyansky, N.F. Zobov, S. V. Shirin, R.J. Barber, J. Tennyson, A 3000K laboratory emission spectrum of water, J. Chem. Phys. 122 (2005) 074307.
[41] M.P. Musculus, K. Kattke, Entrainment waves in diesel jets, SAe Int. J. Engines. 02 (2009) 1170–1193.
[42] L.M. Pickett, J. Manin, C.L. Genzale, D.L. Siebers, M.P. Musculus, C.A. Idicheria, Relationship between diesel fuel spray vapor penetration/dispersion and local fuel mixture fraction, SAe Int. J. Engines. 04 (2011) 764–799.
[43] T. Yao, Y. Pei, A compact skeletal mechanism for n-dodecane with optimized semi-global low-temperature chemistry, Fuel 191 (2017) 339–349.
[44] J.W. Martin, M. Salamanca, M. Kraft, Soot inception: carbonaceous nanoparticle formation in flames, Prog. Energy Combust. Sci. 88 (2022) 100956.
[45] C.J. Mueller, W.J. Pitz, L.M. Pickett, G.C. Martin, D.L. Siebers, C.K. Westbrook, Effects of oxygenates on soot processes in DI diesel engines: experiments and numerical simulations, SAE Trans. 1 (2003) 964–982.
[46] R.L. Axelbaum, C.K. Law, Soot formation and inert addition in diffusion flames, Proc. Combust. Inst. 23 (1991) 1517–1523.